7th EUROMECH Solid Mechanics Conference
J. Ambrosio et.al. (eds.)
Lisbon, Portugal, 7–11 September 2009

MEASUREMENTS OF THE FINITE-TIME SINGULARITY OF THE EULER DISK

R. I. Leine

Institute of Mechanical Systems,
Department of Mechanical and Process Engineering,
ETH Zurich,
CH-8092 Zurich, Switzerland,
remco.leine@imes.mavt.ethz.ch

Keywords: Euler disk, spinning, finite-time singularity, rolling friction, non-smooth dynamics.

Abstract. *This paper is concerned with the dominant dissipation mechanism for a rolling disk in the final stage of its motion. The aim of this paper is to present the various dissipation mechanisms for a rolling disk which are used in the literature in a unified framework. Furthermore, new experiments on the 'Euler disk' using a high-speed video camera and a novel image analysis technique are presented. The combined experimental/theoretical approach of this paper sheds some more light on the dominant dissipation mechanism on the time-scale of several seconds.*

1 INTRODUCTION

If a coin is spun on a table, then we observe a peculiar kind of motion. After a brief initial phase, the coin wobbles/spins while remaining on more or less the same spot. Very slowly the coin loses height. This motion is accompanied by a ringing noise of which the frequency is rapidly increasing and tends to infinity before the motion and sound abruptly stop. This phenomenon is exemplified by the 'Euler disk', a scientific toy consisting of a heavy metal disk on a slightly concave mirror.

The abrupt halt of a spinning disk is often called the 'finite-time singularity' in literature (see for instance [17, 7]). There exists a tremendous amount of literature on the dynamics of the rolling disk. Here, we will only give an overview of the literature on dissipation mechanisms which explain the finite-time singularity and of the literature reporting measurements of this phenomenon.

In a brief article of *Nature*, Moffatt [17] proposed a dissipation mechanism due to viscous drag of the layer of air between the disk and the table. Moffatt showed that, according to this dissipation model, the inclination $\theta(t)$ and precession rate $\dot{\alpha}(t)$ of the disk vary with time according to the power-law

$$\theta(t) \propto (t_f - t)^n, \qquad \dot{\alpha} \propto (t_f - t)^{-\frac{1}{2}n}, \tag{1}$$

with the exponent $n = \frac{1}{3}$. The viscous air drag model of Moffatt was extended by Bildsten [3] to account for boundary layer effects which are expected to occur for larger values of the inclination angle. The derivations of Bildsten reveal an exponent of $n = \frac{4}{9}$. Observations of spinning coins in vacuum led van den Engh *et al.* [22] to suppose that air viscosity is not the dominant dissipation mechanism during the final stage of motion. Moffatt [18] replies that air viscosity is rather insensitive to the pressure and, therefore, that these observations are inconclusive. Moreover, he points out that air drag has a smaller value of n than other dissipation mechanisms and will therefore finally dominate. The article of Moffatt led to an increased interest in the finite-time singularity of the rolling disk and opened the scientific discussion on the responsible dissipation mechanism.

McDonald and McDonald [16] present a dissipation mechanism for rolling friction for which $n = \frac{1}{2}$. Furthermore, the precession rate of a rolling disk is determined experimentally using a flashlight and a phototransistor (5 kS/s) during 10 s. The experimental results of [16] agree well with $n = \frac{1}{2}$.

Stanislavsky and Weron [21] recorded the sound of a rolling disk and analysed the change in the spectrum of the sound between the various stages of motion. No definite conclusions can be drawn from these measurements.

Kessler and O'Reilly [10] study the dynamics of a rolling disk under the influence of sliding, rolling and pivoting dissipation. The sliding friction model in [10] has a static and a dynamic friction coefficient which leads to stick-slip behaviour. The numerical simulations show an asymptotic energy decrease, i.e. the disk does not stop in finite time.

Easwar *et al.* [7] report measurements of the precession rate with a high-speed video camera but do not discuss the details of their measurement technique. The experimental results of [7] agree well with $n = \frac{2}{3}$ which the authors attribute to rolling friction.

Petrie *et al.* [20] conducted measurements of the 'Euler disk' using a normal video camera (30 fps) during 140 s. A strip with markers was glued on top of the disk and the top view of the motion of the disk was recorded. The precession rate and angular velocity around the axis of symmetry were retrieved from image analysis. The inclination angle θ was determined from

the variation of the apparent length of the strip, which resulted in a large experimental error for the inclination angle θ. In [20] it is concluded that the disk rolls without slip during the first 90 s. The measurements are inconclusive for the last 50 s because of the low frame rate.

Caps *et al.* [5] present a rather detailed experimental study of various rolling disks using a high-speed video camera (125-500 fps) and a laser beam during about 10 s. The inclination angle, precession rate and angular velocity around the axis of symmetry of the disk are each measured with a different experimental setup during a different run and, therefore, have not been obtained simultaneously. The experimental results agree with values of n between $\frac{1}{2}$ and $\frac{2}{3}$. Measurements on a torus are believed in [5] to confirm the supposition of van den Engh *et al.* [22] that air drag is only of minor importance.

In Le Saux *et al.*[12] and Leine *et al.* [14], being previous papers of the author, a detailed numerical study has been carried out of a rolling disk under the influence of combined sliding, rolling and pivoting friction. The presented modelling technique includes impact and stick-slip transitions and is able to numerically simulate the transition of the disk from motion to rest and onwards, i.e. the finite-time singularity is within the simulation time-interval.

From the above literature overview we can draw a number of conclusions. Apparently, the general opinion in the scientific community is tending to believe that rolling friction is the dominant dissipation mechanism during the final stage of motion. At this point we have to ask ourselves on which time-scale the final stage of motion is considered. The viscous air drag dissipation might (for highly polished surfaces) be dominant during the last milliseconds, whereas rolling friction can be dominant if we consider the final stage of motion on the time-scale of seconds. The current state-of-the-art experimental results of [5] are only partially satisfactory. The inclination angle, precession rate and angular velocity around the axis of symmetry of the disk are measured, but not simultaneously. Some analytical work exists on the exponent n for various dissipation models, but the results are scattered over the literature and are presented in different notation.

The aim of this paper is twofold. Firstly, the various existing dissipation mechanisms are discussed in a unified framework. This allows for a better comparison of the dissipation mechanisms. Secondly, new experiments on the 'Euler disk' are presented in this paper. The experiments have been conducted with a high-speed video camera (1000 fps) during 10 s. An image analysis technique is presented with which the inclination angle θ and precession rate $\dot{\alpha}$ are obtained simultaneously. The combined experimental/theoretical approach of this paper gives more insight into the dominant dissipation mechanism on the time-scale of several seconds.

The paper is organised as follows. The equations of motion of a rolling disk are reviewed in Section 2. A theoretical analysis of the dissipation-free dynamics of the disk is given in Section 3 and it is shown that the dissipation-free dynamics has a manifold of stationary states for which the inclination remains constant. The stability of these stationary states is analysed using the method of Lyapunov functions by exploiting the integrable structure of the system. Subsequently, all dissipation mechanisms for the rolling disk, which are used in the literature, are discussed in Section 4. The effect of these dissipation mechanisms on the dynamics of the rolling disk is discussed in Section 5. The exponent of the power-law (1) is determined for each dissipation mechanism and an overview of the energy decay for the various dissipation mechanisms is given. The experimental setup and experimental results are presented in Section 6. Finally, conclusions are given in Section 7 and a discussion of the results of this paper in comparison to the results of the existing literature is given.

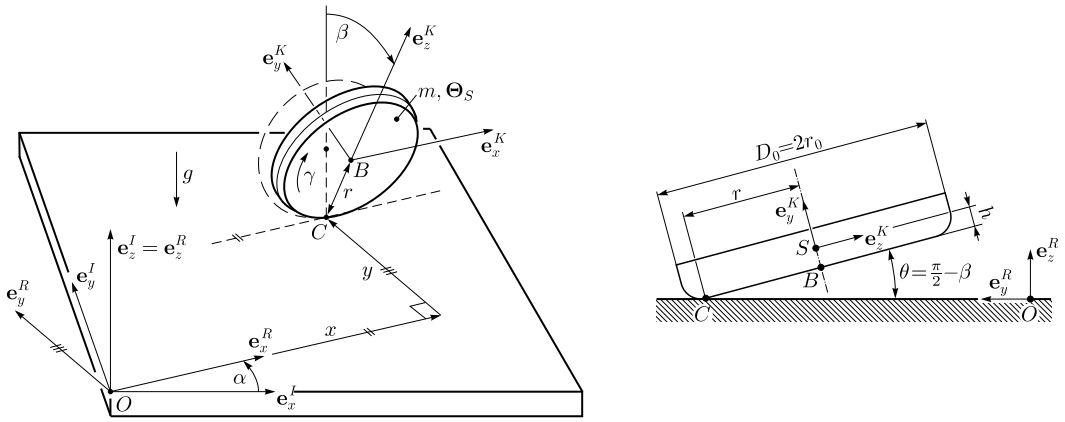

(a) (b)

Figure 1: Rolling disk model: (a) parameterisation, (b) dimensions.

2 ROLLING DISK MODEL

In this section we give a model for a thick rolling disk under the assumption of pure rolling, i.e. rolling without slip, see also [2, 19, 21]. The rigid-body kinematics of a rolling disk are presented in Section 2.1 and the equations of motion are briefly stated in Section 2.2.

2.1 Kinematics

The kinematical model, presented here, describes the mechanical system under consideration as a thick disk submitted to a bilateral geometric constraint at the contact point C (see Figure 1(a)).

An absolute coordinate frame $I = (O, \mathbf{e}_x^I, \mathbf{e}_y^I, \mathbf{e}_z^I)$ is attached to the table. We introduce the frame $R = (O, \mathbf{e}_x^R, \mathbf{e}_y^R, \mathbf{e}_z^R)$ which is obtained by rotating the frame I over an angle α around $\mathbf{e}_z^I$, i.e. $\mathbf{e}_x^R = \cos\alpha\,\mathbf{e}_x^I + \sin\alpha\,\mathbf{e}_y^I$, $\mathbf{e}_y^R = -\sin\alpha\,\mathbf{e}_x^I + \cos\alpha\,\mathbf{e}_y^I$ and $\mathbf{e}_z^R = \mathbf{e}_z^I$. Furthermore, we introduce the frame $K = (B, \mathbf{e}_x^K, \mathbf{e}_y^K, \mathbf{e}_z^K)$ which is obtained by rotating the frame R over an angle β around $\mathbf{e}_x^R$, i.e. $\mathbf{e}_x^K = \mathbf{e}_x^R$, $\mathbf{e}_y^K = \cos\beta\,\mathbf{e}_y^R + \sin\beta\,\mathbf{e}_z^R$ and $\mathbf{e}_z^K = -\sin\beta\,\mathbf{e}_y^R + \cos\beta\,\mathbf{e}_z^R$. Note that frame K is not body-fixed, but moves along with the disk such that $\mathbf{e}_y^K$ is the axis of revolution and the $\mathbf{e}_x^K$-axis remains parallel to the table. The components of a vector $\boldsymbol{r}$ in frame I are expressed as ${}_I\boldsymbol{r}$.

We consider a disk with an (outer) radius r_0 and height $2h$, see Figure 1(b). The disk's bottom surface, with which the disk is in contact with the table, has a rounded edge. The contact point C between the disk and the table therefore runs for small inclination on a tread with constant radius r being slightly smaller than r_0. The geometrical centre of the bottom surface is denoted with B. The centre of mass S is located on the $\mathbf{e}_y^K$ axis at a distance h from B. The disk has mass m and the principal moments of inertia $I_1 = I_2 = \frac{1}{4}mr_0^2 + \frac{1}{12}mh^2$ and $I_3 = \frac{1}{2}mr_0^2$ with respect to the centre of mass S. The inertia tensor in frame K therefore reads as ${}_K\boldsymbol{\Theta}_S = \mathrm{diag}(I_1, I_3, I_1)$. The gravitational acceleration is g in the negative $\mathbf{e}_z^I$ direction. We define a parametrisation of the disk $(x,\ y,\ \alpha,\ \beta,\ \gamma)$, as illustrated in Figure 1(a), which is a minimal set of coordinates with respect to the geometric constraint at the contact point C. In this section, we derive the equations of motion using the coordinates $(x,\ y,\ \alpha,\ \beta,\ \gamma)$ and the angular velocity vector ${}_K\boldsymbol{\Omega} = \begin{bmatrix} {}_K\omega_x & {}_K\omega_y & {}_K\omega_z \end{bmatrix}^{\mathrm{T}}$ expressed in frame K. We will write the components ${}_K\omega_x$, ${}_K\omega_y$ and ${}_K\omega_z$ as ω_x, ω_y and ω_z and omit the subscript K.

First, we derive the angular velocity ${}_K\boldsymbol{\Omega}$ and relate it to the derivatives of the rotational

coordinates $(\alpha,\ \beta,\ \gamma)$:

$$ {}_K\boldsymbol{\Omega} = \dot{\alpha}\ {}_K\mathbf{e}_z^R + \dot{\beta}\ {}_K\mathbf{e}_x^K + \dot{\gamma}\ {}_K\mathbf{e}_y^K = \begin{bmatrix} \dot{\beta} \\ \dot{\alpha}\sin\beta + \dot{\gamma} \\ \dot{\alpha}\cos\beta \end{bmatrix}. \tag{2} $$

Equating the components of ${}_K\boldsymbol{\Omega}$ gives the expressions $\dot{\beta} = \omega_x$, $\dot{\alpha} = \omega_z \sec\beta$ and $\dot{\gamma} = \omega_y - \omega_z \tan\beta$. The rotational velocity of frame K with respect to the inertial frame I can therefore be expressed in frame K as ${}_K\boldsymbol{\omega}_{IK} = \dot{\alpha}\ {}_K\mathbf{e}_z^R + \dot{\beta}\ {}_K\mathbf{e}_x^K$. Similarly, we obtain the rotational velocity of frame R with respect to frame I expressed in frame R as ${}_R\boldsymbol{\omega}_{IR} = \dot{\alpha}\ {}_R\mathbf{e}_z^R = \omega_z \sec\beta\ {}_R\mathbf{e}_z^R$.

The point A is a body-fixed point which is momentarily located at the contact point C and, therefore, momentarily has the coordinates ${}_R\boldsymbol{r}_{OA} = {}_R\boldsymbol{r}_{OC} = \begin{bmatrix} x & y & 0 \end{bmatrix}^{\mathrm{T}}$. The velocity of the body-fixed point A, denoted by $\boldsymbol{v}_A$, momentarily vanishes if pure rolling is assumed. However, the vanishing of the velocity $\boldsymbol{v}_A = \mathbf{0}$ does not imply a vanishing of the acceleration of point A. The point A is therefore not a fixed point with respect to the inertial frame I. Using the distance vector ${}_K\boldsymbol{r}_{AS} = \begin{bmatrix} 0 & h & r \end{bmatrix}^{\mathrm{T}}$, the position of the centre of mass S can be found to be ${}_K\boldsymbol{r}_{OS} = {}_K\boldsymbol{r}_{OA} + {}_K\boldsymbol{r}_{AS} = \begin{bmatrix} x & h + y\cos\beta & r - y\sin\beta \end{bmatrix}^{\mathrm{T}}$. We calculate the velocity $\boldsymbol{v}_S$ of the centre of mass using Euler's differentiation rule:

$$ {}_R\boldsymbol{v}_S = {}_R\dot{\boldsymbol{r}}_{OS} + {}_R\boldsymbol{\omega}_{IR} \times {}_R\boldsymbol{r}_{OS} = \begin{bmatrix} \dot{x} - \omega_z \sec\beta(y + h\cos\beta - r\sin\beta) \\ \dot{y} - h\omega_x \sin\beta - r\omega_x\cos\beta + \omega_z \sec\beta x \\ h\omega_x\cos\beta - r\omega_x\sin\beta \end{bmatrix}. \tag{3} $$

Subsequently, we calculate the velocity of the point A by using the rigid-body equation $\boldsymbol{v}_A = \boldsymbol{v}_S + \boldsymbol{\Omega} \times \boldsymbol{r}_{SA}$. The velocity of the point A has the form $\boldsymbol{v}_A = \gamma_{Tx}\,\mathbf{e}_x^R + \gamma_{Ty}\,\mathbf{e}_y^R$ with

$$ \gamma_{Tx} = \dot{x} - \omega_z \sec\beta(y - r\sin\beta) - \omega_y r, \tag{4} $$

$$ \gamma_{Ty} = \dot{y} + \omega_z \sec\beta\, x, \tag{5} $$

being the relative sliding velocities of the contact point in $\mathbf{e}_x^R$ and $\mathbf{e}_y^R$ direction respectively. The pure rolling condition leads to the two velocity constraints $\gamma_{Tx} = 0$ and $\gamma_{Ty} = 0$.

The velocity of the contact point C over the table equals ${}_R\boldsymbol{v}_C = {}_R\dot{\boldsymbol{r}}_{OC} + {}_R\boldsymbol{\omega}_{IR} \times {}_R\boldsymbol{r}_{OC} = r(\omega_y - \omega_z \tan\beta)\ {}_R\mathbf{e}_x^R$. The velocity of the point C over the rim of the disk equals (under the assumption of pure rolling) the velocity in $\mathbf{e}_x^R$ direction of the point C over the table, i.e.

$$ \gamma_{\mathrm{cont}} = r(\omega_y - \omega_z \tan\beta). \tag{6} $$

2.2 Equations of motion

From the balance of linear and angular momentum we obtain three equations of motion for the three components of the angular velocity vector ${}_K\boldsymbol{\Omega}$

$$ \left(k_1 + 1 + \epsilon^2\right)\dot{\omega}_x - (k_2 + 1 + \epsilon\tan\beta)\,\omega_y\omega_z + \left((k_1 + \epsilon^2)\tan\beta + \epsilon\right)\omega_z^2 = \tilde{g}(\sin\beta - \epsilon\cos\beta) + f_x^{\mathrm{diss}}, \tag{7} $$

$$ (k_2 + 1)\dot{\omega}_y - \epsilon\dot{\omega}_z + (1 + \epsilon\tan\beta)\omega_x\omega_z = f_y^{\mathrm{diss}}, \tag{8} $$

$$ (k_1 + \epsilon^2)\dot{\omega}_z - \epsilon\dot{\omega}_y - \left((k_1 + \epsilon^2)\tan\beta + \epsilon\right)\omega_x\omega_z + k_2\omega_x\omega_y = f_z^{\mathrm{diss}}, \tag{9} $$

with the constants

$$k_1 = \frac{I_1}{mr^2}, \quad k_2 = \frac{I_3}{mr^2}, \quad \epsilon = \frac{h}{r}, \quad \tilde{g} = \frac{g}{r}, \tag{10}$$

and the generalised forces

$$f_x^{\text{diss}} = \frac{1}{mr^2}{}_K M_x^{\text{diss}}, \quad f_y^{\text{diss}} = \frac{1}{mr^2}{}_K M_y^{\text{diss}}, \quad f_z^{\text{diss}} = \frac{1}{mr^2}{}_K M_z^{\text{diss}}. \tag{11}$$

These equations agree for the dissipation-free case ($\boldsymbol{M}^{\text{diss}} = \mathbf{0}$) with those of [1, 2] and for an infinitely thin disk ($\epsilon = 0$) with those of [19, 21].

The kinetic energy in the system is given by

$$\begin{aligned} E_{\text{kin}} &= \frac{1}{2} m_K \boldsymbol{v}_{SK}^{\text{T}} \boldsymbol{v}_S + \frac{1}{2}{}_K \boldsymbol{\Omega}^{\text{T}}{}_K \boldsymbol{\Theta}_{SK} \boldsymbol{\Omega} \\ &= \frac{1}{2}\left(m(r\omega_y - h\omega_z)^2 + m(r^2+h^2)\omega_x^2 + I_1\omega_x^2 + I_3\omega_y^2 + I_1\omega_z^2\right) \\ &= \frac{1}{2} mr^2 \left((\omega_y - \epsilon\omega_z)^2 + (1+\epsilon^2)\omega_x^2 + k_1\omega_x^2 + k_2\omega_y^2 + k_1\omega_z^2\right). \end{aligned} \tag{12}$$

The potential energy of the system is only due to gravity:

$$E_{\text{pot}} = mg(h\sin\beta + r\cos\beta - h) = mr^2\tilde{g}(\epsilon\sin\beta + \cos\beta - \epsilon). \tag{13}$$

In the absence of dissipation it holds that $E = E_{\text{kin}} + E_{\text{pot}} = \text{const.}$

3 THEORETICAL ANALYSIS FOR THE DISSIPATION-FREE CASE

The dynamics of the disk in the absence of dissipation is not only of importance in its own right, but also largely determines the dynamics when the dissipation is small. The three equations of motion (7)-(9) with $\boldsymbol{M}^{\text{diss}} = \mathbf{0}$ form together with $\dot{\beta} = \omega_x$ a four-dimensional autonomous set of differential equations:

$$\dot{\beta} = \omega_x, \tag{14}$$

$$\left(k_1+1+\epsilon^2\right)\dot{\omega}_x - (k_2+1+\epsilon\tan\beta)\,\omega_y\omega_z + \left((k_1+\epsilon^2)\tan\beta+\epsilon\right)\omega_z^2 = \tilde{g}(\sin\beta-\epsilon\cos\beta), \tag{15}$$

$$(k_2+1)\dot{\omega}_y - \epsilon\dot{\omega}_z + (1+\epsilon\tan\beta)\omega_x\omega_z = 0, \tag{16}$$

$$(k_1+\epsilon^2)\dot{\omega}_z - \epsilon\dot{\omega}_y - \left((k_1+\epsilon^2)\tan\beta+\epsilon\right)\omega_x\omega_z + k_2\omega_x\omega_y = 0. \tag{17}$$

The equilibria of these differential equations are studied in Section 3.1 and their stability is addressed in Section 3.2.

3.1 Circular rolling motion

In this section we analyse a particular type of rolling motion in the absence of dissipation. We consider the type of motion $(x_0(t),\, y_0(t),\, \alpha_0(t),\, \beta_0(t),\, \gamma_0(t))$ for which $x_0 = 0$ and $\beta_0 = \text{const.}$ in time $(0 < \beta_0 < \frac{\pi}{2})$. It follows that $\omega_{x0} = 0$ and from (16) and (17) that ω_{y0} = const. and ω_{z0} = const. Furthermore, the sticking constraint $\gamma_{Ty} = 0$ with (5) yields $\dot{y}_0 + \omega_{z0}\sec\beta_0\, x_0 = 0$ from which follows with $x_0 = 0$ that $\dot{y}_0 = 0$ and therefore $y_0 = R = \text{const.}$ Similarly, the

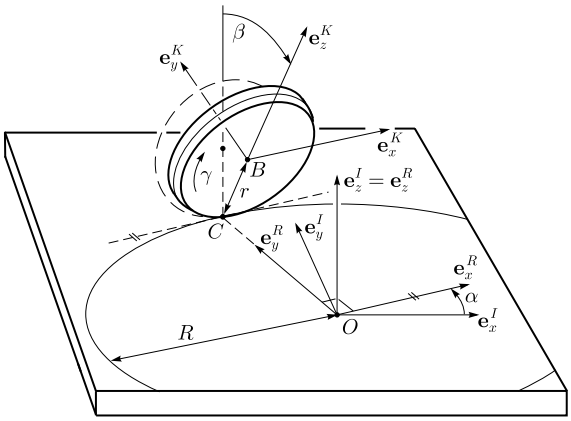

Figure 2: Circular rolling motion.

constraint $\gamma_{Tx} = 0$ with (4) gives $\dot{x}_0 - \omega_{z0} \sec\beta(y_0 - r\sin\beta_0) - \omega_{y0} r = 0$, or, using $\dot{x}_0 = 0$ and $y_0 = R$,

$$\omega_{y0} = \omega_{z0} \sec\beta_0 \left(\sin\beta_0 - \frac{R}{r}\right). \tag{18}$$

Equation (18) is the condition for pure rolling, which means that, for a given time-interval of motion, the arc lengths covered by the contact point C on both the perimeter of the circle (O, R) and the perimeter of the disk are equal. During such a motion, the inclination of the disk β_0 with respect to the vertical $\mathbf{e}_z^I$ and the height of the centre of mass are constant in time. As the contact point C moves on the contour of the disk, it describes on the table a circular trajectory (O, R) of radius R around the origin O of the inertial frame (see Figure 2). In the following we refer to such a type of motion as *circular rolling motion*. A kind of gyroscopic balancing occurs during circular rolling motion. Substitution of $\dot{\omega}_{x0} = 0$ in (15) gives

$$-\left(k_2 + 1 + \epsilon\tan\beta_0\right)\omega_{y0}\omega_{z0} + \left(\left(k_1 + \epsilon^2\right)\tan\beta_0 + \epsilon\right)\omega_{z0}^2 = \tilde{g}(\sin\beta_0 - \epsilon\cos\beta_0), \tag{19}$$

or by using (18)

$$\omega_{z0}^2 = \frac{\tilde{g}(\sin\beta_0 - \epsilon\cos\beta_0)}{\left(k_1 + \epsilon^2\right)\tan\beta_0 + \epsilon - \left(k_2 + 1 + \epsilon\tan\beta_0\right)\sec\beta_0\left(\sin\beta_0 - \frac{R}{r}\right)}, \tag{20}$$

which is the balance between the gyroscopic moment and the gravitational moment. We see from (20) that gyroscopic balancing can only occur if the denominator in (19) is positive and if $\epsilon = \frac{h}{r} < \tan\beta_0$. Furthermore, the friction forces λ_{Tx} and λ_{Ty} have to fulfill the Coulomb sticking condition $\sqrt{\lambda_{Tx}^2 + \lambda_{Ty}^2} < \mu\lambda_N$. The friction forces for circular rolling motion are $\lambda_{Tx} = 0$ and $\lambda_{Ty} = mr\omega_{z0}(\omega_{y0} - \epsilon\omega_{z0})/\cos^2\beta_0$. The four-dimensional system (14)-(17) has embedded in its four-dimensional state-space a two-dimensional manifold $\boldsymbol{q} = (\beta, \omega_x, \omega_y, \omega_z) \in \mathcal{M}$ with boundary, where

$$\mathcal{M} = \left\{ \boldsymbol{q} \mid \omega_x = 0, \omega_z^2 = \frac{\left(k_2 + 1 + \epsilon\tan\beta\right)\omega_y\omega_z + \tilde{g}(\sin\beta - \epsilon\cos\beta)}{\left(k_1 + \epsilon^2\right)\tan\beta + \epsilon}, |\lambda_{Ty}| < \mu m g \right\}. \tag{21}$$

Each point $(\beta_0, \omega_{x0}, \omega_{y0}, \omega_{z0}) \in \mathcal{M}$ is, in the absence of dissipation, an equilibrium of the four-dimensional system (14)-(17) and is what we named a circular rolling motion. As $\mathcal{M}$ consists of equilibria, it is (in the absence of dissipation) an invariant manifold.

Subsequently, we study a particular type of circular rolling motion for which, as the disk is rolling on the table, the centre of mass S remains on the axis $(O, \mathbf{e}_z^I)$ and is therefore immobile with respect to the inertial frame. We call this type of motion *stationary rolling motion*, being characterised by ${}_K\boldsymbol{v}_S = \mathbf{0}$, i.e. $r\omega_{y0} - h\omega_{z0} = 0$ which gives $\omega_{y0} = \epsilon\omega_{z0}$. The gyroscopic balance equation (20) can be written for stationary rolling motion as

$$\omega_{z0}^2 = \frac{\tilde{g}(\sin\beta_0 - \epsilon\cos\beta_0)}{k_1\tan\beta_0 - \epsilon k_2}. \tag{22}$$

The velocity of the contact point $\gamma_{\text{cont}} = r(\omega_{y0} - \omega_{z0}\tan\beta_0)$, given by (6), yields for stationary rolling motion $\gamma_{\text{cont}} = r(\epsilon - \tan\beta_0)\omega_{z0}$. In the limit of $\beta_0 \uparrow \frac{\pi}{2}$ it holds that $\omega_{z0}^2 \to 0$ and $\gamma_{\text{cont}}^2 \to \infty$. The contact point C therefore moves infinitely fast on the circle (O, R) with radius $R \to r$, and moves infinitely fast on the contour of the disk, while the disk does practically not rotate. Stationary rolling motion is a one-dimensional invariant sub-manifold $\mathcal{S} \subset \mathcal{M}$:

$$\mathcal{S} = \left\{ (\beta, \omega_x, \omega_y, \omega_z) \in \mathbb{R}^4 \mid \omega_x = 0, \omega_y = \epsilon\omega_z, \omega_z^2 = \frac{\tilde{g}(\sin\beta - \epsilon\cos\beta)}{k_1\tan\beta - \epsilon k_2} \right\}. \tag{23}$$

The friction forces λ_{Tx} and λ_{Ty} vanish for stationary rolling motion because the centre of mass S does not accelerate for this kind of motion ($\boldsymbol{v}_S = \boldsymbol{a}_S = \mathbf{0}$).

3.2 Lyapunov stability analysis of circular rolling motion

The four-dimensional state space, described by (14)–(17), has a integrable structure. The integrability of the equations of motion of a disk rolling without slip on a rough horizontal surface (no dissipation) was first studied by Chaplygin [6], Appell [1] and Korteweg [11], see [19] for a short overview. The closed form solutions for a rolling disk without dissipation has been used by [19, 2, 4] to study the bifurcations of the stationary motions. Here, we will use the integrability result to study the stability of the stationary motions of the disk using a Lyapunov function.

We will use the notation $(\cdot)' = \mathrm{d}(\cdot)/\mathrm{d}\beta$. The prime derivatives are related to the time-derivatives through

$$\omega_y' = \frac{\mathrm{d}\omega_y}{\mathrm{d}\beta} = \frac{\dot{\omega}_y}{\omega_x}, \qquad \omega_z' = \frac{\mathrm{d}\omega_z}{\mathrm{d}\beta} = \frac{\dot{\omega}_z}{\omega_x}. \tag{24}$$

Following [19], the differential equations (16) and (17) are divided by ω_x and yield a set of differential equations in β for ω_y and ω_z:

$$(k_2+1)\omega_y' - \epsilon\omega_z' + (1 + \epsilon\tan\beta)\omega_z = 0, \tag{25}$$

$$(k_1+\epsilon^2)\omega_z' - \epsilon\omega_y' - \left((k_1+\epsilon^2)\tan\beta + \epsilon\right)\omega_z + k_2\omega_y = 0. \tag{26}$$

Equations (25) and (26) can be combined in a second-order differential equation for $\omega_z(\beta)$:

$$\omega_z'' - \tan\beta\,\omega_z' - \left(\frac{1}{\cos^2\beta} + \frac{k_2(1+\epsilon\tan\beta)}{k_1(k_2+1) + k_2\epsilon^2}\right)\omega_z = 0. \tag{27}$$

The parameters $\omega_y(t_0)$ and $\omega_z(t_0)$ define the initial conditions $\omega_y(\beta(t_0))$ and $\omega_z(\beta(t_0))$ and the values of ω_y and ω_z are therefore completely determined by the value of β. Consequently, we can write $\omega_y = \omega_y(\beta)$ and $\omega_z = \omega_z(\beta)$ as they are functions of β. The four-dimensional state

space therefore reduces to a two-parameter family of second-order systems for $\beta(t)$ (see [19]) and the equation of motion (15) for $\dot{\omega}_x = \ddot{\beta}$ yields

$$\left(k_1+1+\epsilon^2\right)\ddot{\beta} - \left(k_2+1+\epsilon\tan\beta\right)\omega_y\omega_z + \left(\left(k_1+\epsilon^2\right)\tan\beta+\epsilon\right)\omega_z^2 = \tilde{g}(\sin\beta-\epsilon\cos\beta), \quad (28)$$

with $\omega_y = \omega_y(\beta)$ and $\omega_z = \omega_z(\beta)$. We rewrite this autonomous second-order differential equation for β as

$$\left(k_1+1+\epsilon^2\right)\ddot{\beta} + \frac{\partial U}{\partial\beta} = 0, \quad (29)$$

using the potential function

$$U(\beta) = \frac{1}{2}\left((\omega_y-\epsilon\omega_z)^2 + k_2\omega_y^2 + k_1\omega_z^2\right) + \tilde{g}(\epsilon\sin\beta+\cos\beta-\epsilon). \quad (30)$$

The second-order system (28) has equilibria $\beta = \beta_0$ which have to fulfill $U'(\beta_0) = \partial U/\partial\beta|_{\beta=\beta_0} = 0$, and which are circular rolling motions of the four-dimensional system (14)-(17). The stability of these equilibria can be studied with a Lyapunov function

$$V(\bar{\beta},\dot{\bar{\beta}}) = \frac{1}{2}\left(k_1+1+\epsilon^2\right)\dot{\bar{\beta}}^2 + U(\beta_0+\bar{\beta}) - U(\beta_0), \quad (31)$$

with $\bar{\beta} = \beta-\beta_0$ being the difference between β and the equilibrium position β_0. The Lyapunov function V equals the scaled total energy $E = E_{\text{kin}} + E_{\text{pot}}$, given by (12) and (13), shifted with the constant value $U(\beta_0)$, i.e. $V = \frac{1}{mr^2}E - U(\beta_0)$. Hence, the value of V does not change along solution curves of the system because $\dot{V} = 0$. The potential $U(\beta_0+\bar{\beta})$ allows for a Taylor series expansion around β_0

$$U(\beta_0+\bar{\beta}) = U(\beta_0) + U'(\beta_0)\bar{\beta} + \frac{1}{2}U''(\beta_0)\bar{\beta}^2 + \mathcal{O}(\bar{\beta}^3), \quad (32)$$

in which the first-order term vanishes due to the equilibrium condition $U'(\beta_0) = 0$. The Lyapunov function V can therefore be approximated around the origin by

$$V = \frac{1}{2}\left(k_1+1+\epsilon^2\right)\dot{\bar{\beta}}^2 + \frac{1}{2}U''(\beta_0)\bar{\beta}^2 + \mathcal{O}(\bar{\beta}^3). \quad (33)$$

Hence, the Lyapunov function V is locally positive definite if $U''(\beta_0) > 0$ and the equilibrium position β_0 is therefore Lyapunov stable if $U''(\beta_0) > 0$ is fulfilled. For small $\bar{\beta}$ it holds that

$$\left(k_1+1+\epsilon^2\right)\ddot{\bar{\beta}} + U''(\beta_0)\bar{\beta} = 0, \quad (34)$$

from which we see that the disk swings for small amplitudes with a nutational frequency

$$\omega_{\text{nutation}}^2 = \frac{U''(\beta_0)}{k_1+1+\epsilon^2}. \quad (35)$$

The second derivative of the potential U can tediously be obtained by solving ω_y' and ω_z' from (25) and (26). The derivation greatly simplifies for $\epsilon = 0$, i.e. if the disk is infinitely thin, and under the assumption of stationary rolling motion ($\omega_{y0} = 0$) and the result is

$$U''(\beta_0) = \left(k_1(1+3\tan^2\beta_0)+1\right)\omega_{z0}^2 - \tilde{g}\cos\beta_0 = \left(3\tan^2\beta_0 + \frac{1}{k_1}\right)\tilde{g}\cos\beta_0, \quad (36)$$

which is positive ($0 < \beta < \pi/2$). Consequently, stationary rolling motion is stable for an infinitely thin disk and has a nutational frequency (35) given by

$$\omega_{\text{nutation}}^2 = \frac{(3k_1\tan^2\beta_0+1)\,\tilde{g}\cos\beta_0}{k_1(k_1+1)}. \quad (37)$$

4 DISSIPATION MECHANISMS

In this section we discuss a number of dissipation mechanisms of a rolling disk. First, we discuss two types of rolling friction and pivoting friction (drilling friction). Subsequently, we pay some attention to sliding friction of the disk over the table. Finally, viscous air drag models are addressed. For the formulation of dry friction laws as set-valued force-laws (i.e. inclusions) we refer to [8, 15].

4.1 Classical rolling friction

Bodies in contact can experience a resistance against rolling over each other. At this point we have to ask ourselves what we exactly mean when we say that bodies 'roll' over each other [15]. We may call 'rolling' the movement of the contact point over the surface of one of the bodies (here already lies some ambiguity). A resistance against such a type of movement will be called contour friction and is discussed in Section 4.2. Usually, the term rolling is associated with resistance against a difference in angular velocity components of the contacting bodies which are tangential to the contact plane (see for instance [9]). This will be called classical rolling friction. Contour friction and classical rolling friction may be identical to each other or be essentially different, depending on the type of system. For instance, if a planar wheel rolling over a flat table is considered, then the two types of rolling friction yield the same kind of dissipation mechanism, because the velocity of the contact point over the contour of the wheel is directly proportional to the angular velocity of the wheel. However, the two types of rolling friction are essentially different if we consider a three-dimensional disk rolling on a table.

The classical rolling friction law, applied to the rolling disk, describes a frictional moment in the horizontal plane of the table as a function of the projection of the angular velocity on the horizontal plane. The angular velocity $\boldsymbol{\Omega}$ of the disk has the components ${}_R\omega_x = \omega_x$ and ${}_R\omega_y = \omega_y \cos\beta - \omega_z \sin\beta$ around the $\mathbf{e}_x^R$ and $\mathbf{e}_y^R$ axes. For the motion of a rolling disk we can assume that the frictional moment is much smaller around the $\mathbf{e}_x^R$ axis than around the $\mathbf{e}_y^R$ axis. A dry classical rolling friction law (for the $\mathbf{e}_y^R$ axis) therefore reads as

$$M_{\text{roll}} \in -\mu_{\text{roll}} \lambda_N r \,\text{Sign}(\omega_{\text{roll}}), \tag{38}$$

with the friction coefficient μ_{roll} and the rolling angular velocity $\omega_{\text{roll}} = \boldsymbol{\Omega} \cdot \mathbf{e}_y^R = {}_R\omega_y = \omega_y \cos\beta - \omega_z \sin\beta$. Similarly, we can consider a viscous classical rolling friction model, described by $M_{\text{roll}} = -c_{\text{roll}}\omega_{\text{roll}}$. The classical rolling friction moment M_{roll} induces a generalised moment $\boldsymbol{M}^{\text{diss}} = M_{\text{roll}}\mathbf{e}_y^R$ in the equations of motion (7)-(9).

4.2 Contour friction

Contour friction is a resisting moment against the movement of the contact point C over the rim of the disk [12, 15]. We prefer to consider a contour angular velocity $\omega_{\text{cont}} = \frac{\gamma_{\text{cont}}}{r}$. A dry contour friction law therefore reads as

$$M_{\text{cont}} \in -\mu_{\text{cont}} \lambda_N r \,\text{Sign}(\omega_{\text{cont}}), \tag{39}$$

where μ_{cont} is a dimensionless friction coefficient. Similarly, we can consider a viscous contour friction model, described by

$$M_{\text{cont}} = -c_{\text{cont}}\omega_{\text{cont}}. \tag{40}$$

The contour friction moment M_{cont} induces a virtual power $\delta\omega_{\text{cont}} M_{\text{cont}} = (\delta\omega_y - \delta\omega_z \tan\beta) M_{\text{cont}}$ which equals the virtual power $\delta\omega_{xK} M_x^{\text{diss}} + \delta\omega_{yK} M_y^{\text{diss}} + \delta\omega_{zK} M_z^{\text{diss}}$ of the generalised forces.

Considering arbitrary variations $\delta\omega_x$, $\delta\omega_y$ and $\delta\omega_z$ we conclude that the generalised moment due to contour friction reads as $\boldsymbol{M}^{\text{diss}} = M_{\text{cont}}\mathbf{e}_y^K - M_{\text{cont}}\tan\beta\mathbf{e}_z^K$.

4.3 Pivoting friction

Pivoting friction [13] is a frictional moment which resists a pivoting angular velocity ω_{pivot} of the disk around the contact point C. Pivoting friction for the rolling disk has been studied in [12]. If the pivoting angular velocity is large, then a coupling with sliding friction can exist. This coupling is modelled by the Coulomb-Contensou friction law [15], which is not of importance in this context and will not be considered here. A dry pivoting friction law reads as

$$M_{\text{pivot}} \in -\mu_{\text{pivot}}\lambda_N r\,\text{Sign}(\omega_{\text{pivot}}), \tag{41}$$

with the pivoting velocity $\omega_{\text{pivot}} = {}_I\omega_z = \sin\beta\omega_y + \cos\beta\omega_z$. Similarly, we can consider a viscous pivoting friction model $M_{\text{pivot}} = -c_{\text{pivot}}\omega_{\text{pivot}}$. The pivoting friction moment M_{pivot} induces a generalised moment $\boldsymbol{M}^{\text{diss}} = M_{\text{pivot}}\mathbf{e}_z^I = M_{\text{pivot}}\sin\beta\,\mathbf{e}_y^K + M_{\text{pivot}}\cos\beta\,\mathbf{e}_z^K$.

4.4 Sliding friction

The equations of motion (7)-(9) have been derived under the assumption that the disk purely rolls over the table ($\gamma_{Tx} = \gamma_{Ty} = 0$), i.e. there is no sliding in the $\mathbf{e}_x^R$ and $\mathbf{e}_y^R$ direction of the contact point. The dissipation due to a resistance against sliding of the contact point over the table, which is called radial slippage in [16], can therefore not be studied with the equations of motion (7)-(9). A detailed numerical model of a rolling disk which also includes sliding friction has been presented in [12]. In order to study the effect of sliding friction analytically one would have to consider the equations of motion of a 'sliding disk', as have been discussed in [19], together with friction forces λ_{Tx} and λ_{Ty} (see [2]) and a Coulomb or viscous friction law. However, the friction forces λ_{Tx} and λ_{Ty} vanish for stationary rolling motion. It is therefore concluded in [16] that sliding friction is not able to dissipate energy if the disk is in a state of stationary rolling motion.

4.5 Viscous air drag

Moffatt [17] proposes a dissipation mechanism due to viscous drag of the layer of air between the disk and the table. During the final stage of motion the inclination $\theta(t) = \pi/2 - \beta(t)$ is very small and the air is squeezed between the almost parallel surfaces of the disk and table. The maximal gap between the disk and the table has a height being proportional to $\sin\theta \approx \theta$. Moffatt assumes that the horizontal velocity of the air u_H is proportional to the precession speed $\dot{\alpha}$. Furthermore, assuming a no-slip condition for the layer of air on the table and disk, he deduces that the layer of air has a shear proportional to $\frac{\partial u_H}{\partial z} \propto \dot{\alpha}/\theta$. Hence, assuming linear viscosity of the air, the disk experiences a moment $M_{\text{drag}} = -c_{\text{drag}}\dot{\alpha}/\theta$ around the $\mathbf{e}_z^I$ axis. The coefficient c_{drag} depends on the viscosity of the air and the radius of the disk. The viscous air drag model induces a generalised moment $\boldsymbol{M}^{\text{diss}} = M_{\text{drag}}\mathbf{e}_z^I$.

The viscous air drag model of Moffatt has been extended by Bildsten [3] to account for boundary layer effects which occur for larger values of the inclination angle. Bildsten [3] argues that the viscous dissipation does not extend over the whole gap for larger values of the inclination θ but only occurs in boundary layers on the disk and table. The width of these boundary layers is proportional to $\delta \propto \dot{\alpha}^{-\frac{1}{2}}$ and the shear is therefore proportional to $M_{\text{drag}} \propto \frac{\partial u_H}{\partial z} \propto \dot{\alpha}/\delta \propto \dot{\alpha}^{\frac{3}{2}}$.

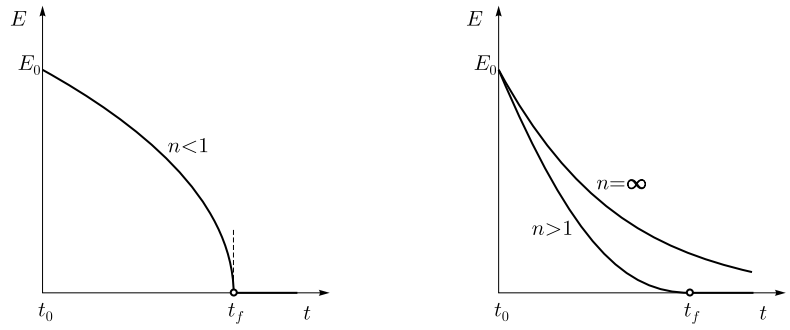

Figure 3: Energy decay for (a) $n < 1$ and (b) $n > 1$.

5 The finite-time singularity

The dissipation mechanisms presented in Section 4 lead to a monotonous decay of the energy and therefore ultimately to a decay of the inclination angle $\theta(t)$. The question of interest now is: which of these dissipation mechanisms predicts a finite-time singularity, or, in other words, an abrupt halt of the motion in a finite time? Furthermore, we would like to know how the time-history of $\theta(t)$ looks like for each of these dissipation mechanisms, e.g. the power-law relationship (1) with a certain exponent n. In this section we give analytical approximations for the energy decay of a rolling disk for the dissipation mechanisms presented in Section 4. The energy decay is studied during the final stage of motion which motivates the following standing assumptions for the type of motion

A.1 The centre of mass is assumed to be almost immobile, i.e. stationary rolling motion holds and $\omega_y = \epsilon\omega_z$.

A.2 We assume that the kinetic energy associated with ω_x is small compared to the potential energy, i.e. $\frac{1}{2}(1+k_1)\omega_x^2 \ll \tilde{g}\theta$.

A.3 We assume $\theta = \pi/2 - \beta$ to be close to 0 and neglect terms of order $\mathcal{O}(\theta^2)$ with respect to terms of order $\mathcal{O}(1)$.

A.4 We neglect terms of order $\mathcal{O}(\epsilon^2)$ and $\mathcal{O}(\epsilon\theta)$ with respect to terms of order $\mathcal{O}(1)$.

Once an approximation for the energy decay is found, one has to check whether the above assumptions are met. Using the assumptions A.1–A.4, we approximate the total energy $E = E_{\mathrm{kin}} + E_{\mathrm{pot}}$, see (12) and (13), by the expression

$$E = \frac{1}{2}mr^2\left(k_1\omega_z^2 + 2\tilde{g}\theta\right), \tag{42}$$

in which only the major terms have been taken into account. Using the assumptions A.1, A.2 and A.4 we approximate ω_z with the gyroscopic balance equation (22) and only retain leading terms

$$\omega_z^2 = \frac{\tilde{g}(\sin\beta - \epsilon\cos\beta)}{k_1\tan\beta - \epsilon k_2} \approx \frac{\tilde{g}(1-\epsilon\theta)}{k_1\theta^{-1} - \epsilon k_2} \approx \frac{\tilde{g}}{k_1}\theta. \tag{43}$$

The assumption of gyroscopic balancing for quasi-stationary motion is called the 'adiabatic approximation' in [17]. By substitution of (43) in (42), the total energy of the system can be

approximated with

$$E = \frac{3}{2} m r^2 \tilde{g} \theta, \tag{44}$$

from which we see that the energy E is proportional to the inclination θ. In the following, we express for the various kinds of dissipation mechanisms the dissipative power $\dot{E}$ as a function of energy, i.e. $\dot{E} = f(E)$ for $E > 0$. The power–energy relation gives a scalar differential equation which approximates the time-evolution of the system during the final stage of motion.

If we choose a dry contour friction law, as introduced in Section 4.2, then the dissipation rate reads as

$$\dot{E} = -\mu_{\mathrm{cont}} \lambda_N r |\omega_{\mathrm{cont}}|. \tag{45}$$

The assumptions A.2 and A.3 allow us to approximate the normal contact force with $\lambda_N = mg$. We now have to express ω_{cont} as a function of E. Using (6), (43) and (44) it holds that

$$\omega_{\mathrm{cont}}^2 = (\omega_y - \omega_z \tan\beta)^2 \approx \left(\epsilon - \frac{1}{\theta}\right)^2 \omega_z^2 \approx \frac{\tilde{g}}{k_1}\frac{1}{\theta} \approx \frac{3mr^2\tilde{g}^2}{2k_1}\frac{1}{E}. \tag{46}$$

The dissipation rate $\dot{E}$ for dry contour friction, see (45), can therefore be expressed as

$$\dot{E} = -\frac{a}{\sqrt{E}}, \quad \text{with } a = \mu_{\mathrm{cont}} \left(\frac{3\tilde{g}}{2k_1}\right)^{\frac{1}{2}} \left(mr^2\tilde{g}\right)^{\frac{3}{2}}. \tag{47}$$

For an arbitrary initial condition $E(t_0) = E_0 > 0$, the differential equation (47) obeys the solution

$$E(t) = \left(E_0^{\frac{3}{2}} - \frac{3}{2}a(t - t_0)\right)^{\frac{2}{3}} \quad \text{for } t_0 \le t \le t_f, \tag{48}$$

which shows a decrease to zero in a finite time $t_f - t_0 = 2E_0^{\frac{3}{2}}/(3a)$ similar to Figure 3(a). From the energy $E(t)$ we can calculate $\theta(t)$ using (44) which gives

$$\theta(t) = \left(\theta_0^{\frac{3}{2}} - \sqrt{\frac{\tilde{g}}{k_1}}\mu_{\mathrm{cont}}(t - t_0)\right)^{\frac{2}{3}}. \tag{49}$$

Now that the solution $\theta(t)$ is known, we can check the validity of the assumption A.2. Evaluation of the condition $\frac{1}{2}(1 + k_1)\dot{\omega}_x^2 \ll \tilde{g}\theta$ by substitution of (49) gives the condition $t_f - t = \tau \gg \tau_c$ with the critical inverse time τ_c

$$\tau_c = \left(\frac{2}{9}(k_1 + 1)\right)^{\frac{3}{4}} k_1^{-\frac{1}{4}} \left(\frac{\mu_{\mathrm{cont}}}{\tilde{g}}\right)^{\frac{1}{2}}. \tag{50}$$

If we consider a viscous contour friction model $M_{\mathrm{cont}} = -c_{\mathrm{cont}}\omega_{\mathrm{cont}}$ (40), then the dissipation rate reads as $\dot{E} = -c_{\mathrm{cont}}\omega_{\mathrm{cont}}^2$. Using the approximation (46), similar to the above analysis, we deduce that

$$\dot{E} = -\frac{a}{E}, \quad \text{with } a = \frac{3}{2}\frac{m\tilde{g}^2 r^2}{k_1} c_{\mathrm{cont}}. \tag{51}$$

friction type	diff. equation	energy profile	exponent
contour friction:			
dry	$\dot{E} = -aE^{-\frac{1}{2}}$	$E(t) = \left(E_0^{\frac{3}{2}} - \frac{3}{2}a(t-t_0)\right)^{\frac{2}{3}}$	$n = \frac{2}{3}$
viscous	$\dot{E} = -aE^{-1}$	$E(t) = (E_0^2 - 2a(t-t_0))^{\frac{1}{2}}$	$n = \frac{1}{2}$
class. rolling friction:			
dry	$\dot{E} = -aE^{\frac{1}{2}}$	$E(t) = \left(\sqrt{E_0} - \frac{a}{2}(t-t_0)\right)^2$	$n = 2$
viscous	$\dot{E} = -aE$	$E(t) = E_0 e^{-a(t-t_0)}$	$n = \infty$
pivoting friction:			
dry	$\dot{E} = -aE^{\frac{1}{2}}$	$E(t) = \left(\sqrt{E_0} - \frac{a}{2}(t-t_0)\right)^2$	$n = 2$
viscous	$\dot{E} = -aE$	$E(t) = E_0 e^{-a(t-t_0)}$	$n = \infty$
sliding friction:	$\dot{E} = 0$	$E(t) = E_0$	$n = 1$
viscous air drag:			
Moffatt	$\dot{E} = -aE^{-2}$	$E(t) = (E_0^3 - 3a(t-t_0))^{\frac{1}{3}}$	$n = \frac{1}{3}$
Bildsten	$\dot{E} = -aE^{-\frac{5}{4}}$	$E(t) = \left(E_0^{\frac{9}{4}} - \frac{9}{4}a(t-t_0)\right)^{\frac{4}{9}}$	$n = \frac{4}{9}$

Table 1: Power–energy relations for various friction models.

For an arbitrary initial condition $E(t_0) = E_0$, the differential equation (51) obeys the solution

$$E(t) = \left(E_0^2 - 2a(t-t_0)\right)^{\frac{1}{2}} \quad \text{for } t_0 \leq t \leq t_f, \tag{52}$$

which shows a decrease to zero in a finite time $t_f - t_0 = E_0^2/(2a)$.

The power–energy relations can be deduced for all other dissipation mechanisms presented in Section 4: dry/viscous classical rolling friction, dry/viscous pivoting friction, sliding friction and the viscous air drag models of Moffatt [17] and Bildsten [3]. The results are summarised in Table 1 and the exponent n is given in the last column. A sketch of the energy profiles depending on n are shown in Figure 3. Viscous classical rolling friction and viscous pivoting friction have an exponent $n = \infty$ as can be seen from the property $e^x = \lim_{n\to\infty}(1 + \frac{x}{n})^n$ of the exponential function. In Section 4.4 we concluded that sliding friction is not able to dissipate energy if the disk is in a state of stationary rolling motion and it therefore holds that $\dot{E} = 0$ under assumption A.1. The dissipation for sliding friction can be put in the form $\dot{E} = -aE^0$ with $a = 0$ and sliding friction therefore has a (theoretical) exponent $n = 1$.

We conclude that viscous classical rolling friction and viscous pivoting friction predict an asymptotic behaviour of the energy profile whereas sliding friction predicts no energy dissipation at all. All other dissipation mechanisms, discussed here, lead to a decrease of the energy in finite time. However, dry classical rolling friction and dry pivoting friction predict a parabolic decay of the energy ($n = 2$) and therefore not an abrupt halt of the motion. The viscous air drag model of Moffatt predicts the smallest value of the exponent n.

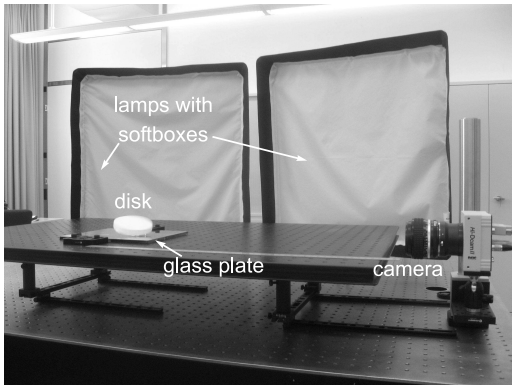

Figure 4: Experimental setup.

6 EXPERIMENTAL ANALYSIS

Experiments have been conducted on the 'Euler disk' (a scientific toy of Tangent Toy) using a high-speed video camera. The experimental setup and measurement technique are presented in Section 6.1. The experimental results are discussed in Section 6.2 and a comparison is given with the theoretical results of the previous sections. The geometric data and inertia properties of the 'Euler disk' are $D_0 = 2r_0 = 75.5$ mm, $D = 2r = 70.0$ mm, $H = 2h = 13$ mm, $m = 0.4499$ kg, $I_1 = \frac{1}{4}mr_0^2 + \frac{1}{12}mh^2$, $I_3 = \frac{1}{2}mr_0^2$ and $g = 9.81$ m/s^2.

6.1 Experimental setup and measurement method

The experimental setup (Figure 4) consists the disk which is spun on a glass (or aluminium) base-plate being fixed to the supporting table. A high-speed camera is positioned such that it records the side-view of the spinning disk. Two lamps with softboxes provide diffuse light in order to avoid shadows. The top and side of the disk have been painted white for better reflection. The high-speed video camera (NAC, Hi-Dcam II) has been used at a framerate of 1000 fps with a shutter time of 1/1000 s and a resolution of 1060×348 pixels. The disk is put in motion by hand and the measurement is stopped manually when the motion of the disk has ceased. The last 10000 frames, which corresponds to 10 s recording time, are stored on the computer board.

The data is analysed frame-by-frame in a post-processing phase using a dedicated MATLAB program written by the author. First, the frame is converted to a black-and-white image using an edge-detection algorithm (Image Processing Toolbox). The rim of the top surface of the disk is in this image visible as an ellipse if the surface is in view of the camera, or as the upper segment of an ellipse if the surface is not in view of the camera. Figures 5 shows a frame before and after post-processing. In a second step, a number of points on the rim of the disk are located. An ellipse is fitted on these points, which is a linear least-square problem. This leads to a first estimate for the semi-major and semi-minor axes of the top surface of the disk and for the position of its geometric centre. This first estimation for the parameters of the ellipse is already very good if the top surface in view of the camera and the whole ellipse is visible. However, if the top surface is not in view of the camera, then only the upper part of the rim is visible and the fitted ellipse can be cumbersome. The semi-major axis should be equal to the diameter of the disk of which the size in pixels is known at forehand. A second fitting procedure is carried out with a pre-specified semi-major axis. This leads to a nonlinear least-square problem, which is solved using the first estimation as initial guess. This final estimation

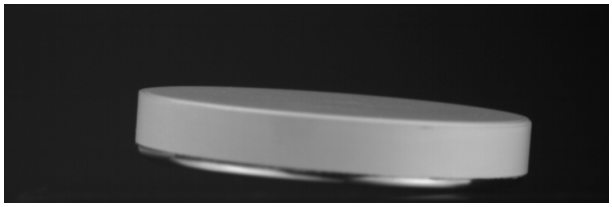

(a)

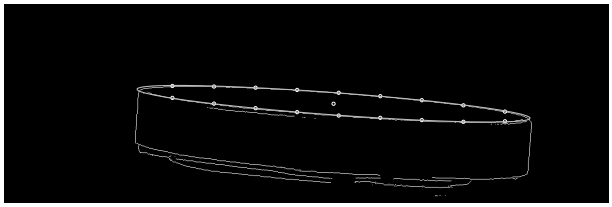

(b)

Figure 5: Frame before processing (a) and after processing (b).

of the ellipse is satisfactory for all frames. The parameters of the ellipse provide two pieces of information: the inclination angle θ of the disk and the precession angle α. No information is obtained about the angle γ.

Figure 5(b) shows the post-processed frame. Eighteen points (indicated with small circles) have been found on the rim of the top surface. The fitted ellipse is shown with a larger line-thickness. The described post-processing technique of the images which fits an ellipse on the top surface has the advantage that it gives a reasonably accurate result even if the contour of the disk is blurred, because the method uses a number of points, which averages out uncertainties. The blurring in the images prohibits techniques which simply determine the inclination angle by finding the highest point of the disk.

6.2 Experimental results

A number of measurements have been done with both glass and aluminum flat base-plates. The results were always qualitatively similar, with the distinction that the spinning times on an aluminum plate were much smaller. Here, we discuss only one measurement with a glass base-plate.

Figure 6(a) shows the time-history of the measured inclination angle $\theta(t)$. We observe that the disk comes to an abrupt halt at $t = t_f = 9.61$ s after which $\theta(t) = 0$, i.e. the disk lies flat on the base-plate. We also see that the motion of the disk consists of a 'slow motion' with a superimposed high-frequency oscillation. The slow motion of the inclination θ shows a kind of 'square-root' behaviour, i.e. the slope tends to minus infinity just before the motion ceases. This is often called the 'finite-time singularity' in literature.

Figure 6(b) shows $\log(\theta)$ as a function of $\log(\tau)$, where $\tau = t_f - t$ is the inverse time and $\log(x)$ denotes the natural logarithm of x. The 'finite-time singularity' occurs for $\tau = 0$ s. The slope of the curve in Figure 6(b) varies from $\frac{2}{3}$ for large τ to $\frac{1}{2}$ for small τ. We therefore read from Figure 6(b) that for different time-intervals it holds that

$$\theta(\tau) \propto \tau^n, \tag{53}$$

with $n = \frac{2}{3}$ or $n = \frac{1}{2}$. Furthermore, the curve in Figure 6(b) crosses the vertical axis $\log \tau = 0$ at the value -3.5 and it therefore approximately holds that $\theta(\tau) = 0.0302 \cdot \tau^n$. Assuming dry contour friction and using (49) and (50), we obtain the estimate $\mu_{\text{cont}} = 1.7 \cdot 10^{-4}$ for the

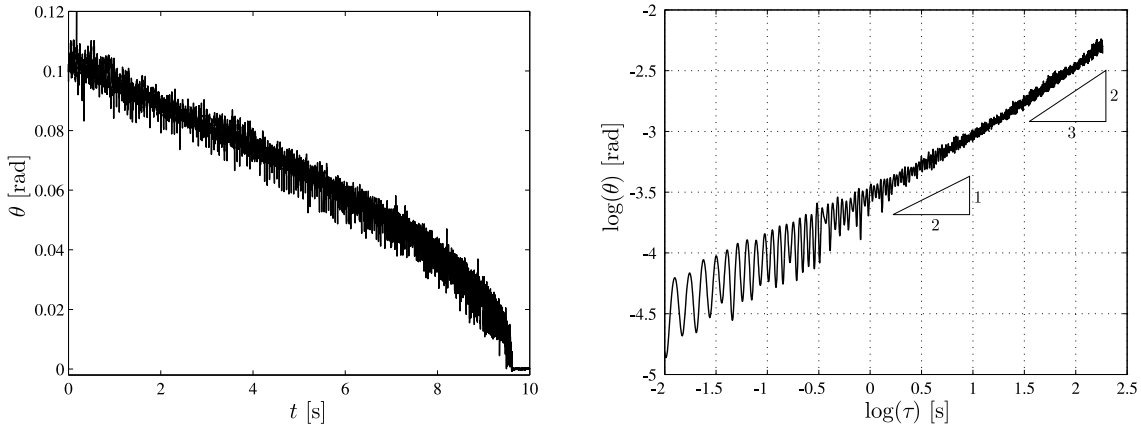

(a) Time-history (b) Double-logarithmic plot vs. $\tau = t_f - t$

Figure 6: Measured inclination angle θ.

contour friction coefficient and $\tau_c = 4.2{\cdot}10^{-4}$ s for the critical time. Similarly, assuming viscous contour friction, we obtain the estimate $c_{\text{cont}} = 1.1 \cdot 10^{-7}$ Nms and $\tau_c = 1.5 \cdot 10^{-3}$ s. Hence, according to the theoretical analysis of Section 5, the assumption of gyroscopic balancing can no longer be expected to hold during the last milliseconds before the end of motion.

The angular velocity $\omega_z = \dot{\alpha} \cos\beta$ is obtained from $\beta(t) = \frac{\pi}{2} - \theta(t)$ and numerical differentiation of $\alpha(t)$ with a low-pass filtering (50 Hz cut-off frequency). Furthermore, a semi-analytical theoretical prediction of ω_z is obtained using equation (22) and the measured values of $\beta(t)$. Equation (22) assumes that the disk is in a state of stationary rolling motion. Figure 7(a) shows the 'measured' angular velocity ω_z as a solid line and the theoretical prediction with equation (22) by small circles. We see that the two estimations of ω_z agree very well.

The high-frequency content of the signal $\theta(t)$ is analysed using a moving-window discrete fast Fourier transform. At each discrete time-instant a window of 2000 samples is taken (2 seconds), centred around that time-instant. Each window is analysed by a 2^{12} point FFT and the frequency corresponding to the highest peak in the spectral density curve is determined. This frequency, which is shown in Figure 7(b) by a solid line, is a measured estimate for the nutational frequency ω_{nutation}. The described method has a resolution of $2\pi \cdot 1000/2^{12} = 1.53$ rad/s, which explains the stairs of the solid line in Figure 7(b). Only the first 5 seconds have been shown because the measured estimate for ω_{nutation} becomes unreliable when the slope of $\theta(t)$ is too large and varies too much during 2 seconds. A semi-analytical theoretical prediction of ω_{nutation} is obtained using equation (35) together with (25), (26), $\omega_y(t) = \epsilon\omega_z(t)$ and the measured values of $\beta(t)$ and $\omega_z(t)$. The theoretical prediction of $\omega_{\text{nutation}}(t)$ assumes that the disk in a state of stationary rolling motion. The theoretical prediction of $\omega_{\text{nutation}}(t)$ is shown in Figure 7(b) as small circles. The two estimates of $\omega_{\text{nutation}}(t)$ agree reasonably well.

From this experiment we can draw a number of conclusions about the motion and dissipation mechanism during the final stage of motion of a rolling disk. We first discuss the conclusions about the type of motion and then discuss the dissipation mechanism.

The good agreement between experimentally obtained values for ω_z and ω_{nutation} with theoretically estimates under the assumption of stationary rolling motion indicates that the disk is approximately in a state of stationary rolling motion. That is to say, the disk is during the final stage of motion in the neighbourhood of a quasi-equilibrium state for which the centre of mass is almost immobile. The dissipation in the system causes the quasi-equilibrium state to slowly

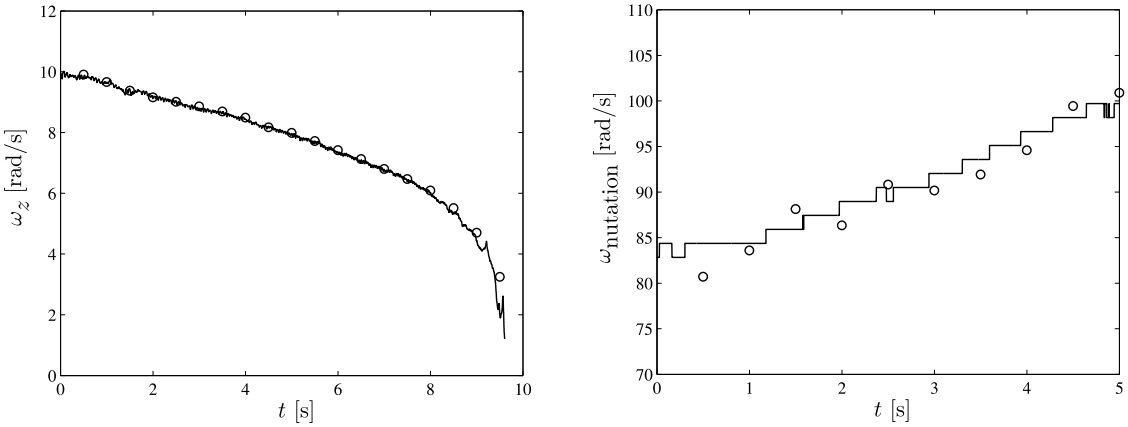

(a) Angular velocity ω_z vs. time

(b) Nutation frequency vs. time

Figure 7: Measured angular velocity and nutation frequency (solid lines) and semi-analytical theoretical predictions ($\circ$ symbols).

change over time. Apparently, the state of the disk slides almost along the one-dimensional sub-manifold $\mathcal{S}$ of stationary rolling motion equilibrium states given by (23). The motion of the disk consists of the superposition of the slowly varying quasi-equilibrium state and a high frequency nutational oscillation.

We now come to conclusions about the energy decay and the responsible dissipation mechanism. The theoretical results in Section 5 have been derived under the standing assumptions A.1–A.4. The discussion in the previous paragraph indicate that assumption A.1 is fulfilled. The measured decay of the inclination angle θ over time shown in Figure 6 indicates that the inclination is proportional to the fractional power of the inverse time τ. Assumption A.2 is therefore not fulfilled for very small τ, i.e. for t close to t_f, because $\omega_x = -\dot{\theta}$ tends to infinity. However, if we do not consider the last fraction of a second before the finite-time singularity and consider the final stage of motion of the disk on a time-scale of seconds, then we can reasonable say that assumption A.2 is fulfilled. Clearly, also assumptions A.3 and A.4 are fulfilled, because $\epsilon = 0.1875$ and $\theta < 0.12$ rad. Hence, under the validity of these assumptions, equation (44) expresses the proportionality between the total energy E and the inclination θ, which in turns leads to the proportionality

$$E(\tau) \propto \tau^n, \tag{54}$$

with $n = \frac{2}{3}$ for large τ and $n = \frac{1}{2}$ for small τ.

7 CONCLUSIONS

A literature overview of experiments on the rolling disk has been given in Section 1. The publications which give an experimental value for the exponent n are listed in Table 2. It can be seen that all publications, including the results of Section 6, report the exponents $n = \frac{1}{2}$ and/or $n = \frac{2}{3}$.

Various dissipation mechanisms for the rolling disk have been discussed in Section 5 and the corresponding energy profiles and exponents are listed in Table 1. The dry contour friction dissipation mechanism leads to the exponent $n = \frac{2}{3}$, whereas a viscous contour friction dissipation mechanism has the exponent $n = \frac{1}{2}$. It is therefore tempting to make the quick conclusion that dry contour friction prevails at the beginning of the stationary rolling phase and that viscous

McDonald and McDonald [16]	$n = \frac{1}{2}$
Easwar *et al.* [7]	$n = \frac{2}{3}$
Caps *et al.* [5]	$n = \frac{1}{2}, \frac{2}{3}$
this paper	$n = \frac{1}{2}, \frac{2}{3}$

Table 2: Experimental results on the exponent n.

contour friction prevails during the last one or two seconds before the motion stops. The contour velocity γ_{cont} tends to infinity if τ approaches zero, which can explain why viscous contour friction prevails for small τ (large contour velocity) and dry contour friction prevails for large τ (small contour velocity). However, we should be careful with definite statements about the nature of the dissipation mechanism. All we can really say is that a dissipation mechanism of dry and viscous contour friction can well explain the observed experimental results, but other dissipation mechanisms might exist which lead to the same exponent n in the energy decay relationship.

In Section 1 it was mentioned that the considered time-scale is of importance when speaking about *the* dominant dissipation mechanism for the rolling disk. Moffatt [18] suggests that viscous air drag has to prevail at the very end of the motion as the associated exponent is smaller than, for instance, the exponent of contour or classical rolling friction. However, the exponent for the various dissipation mechanisms, including viscous air drag, have been derived under the assumption of gyroscopic balancing. This puts a lower bound τ_c on the inverse time τ in the order of milliseconds, i.e. at the very end of the motion. Moreover, the effect of the surface roughness and contamination may play a role when the inclination angle and gap between disk and table become very small. It is therefore questionable whether viscous air drag will finally become dominant if the surfaces are not highly polished. Furthermore, the experimental results do not have a sufficient resolution to reveal the dynamics at extremely small inclination angles ($\theta < 0.01$ rad). The question of the dominant dissipation mechanism during the last fraction of a second, which is perhaps of less practical interest, therefore remains unanswered.

Consequently, the experimental evidence and theoretical analysis presented in this paper do not prove but strongly suggest that dry and viscous contour friction are the dominant dissipation mechanisms for the finite-time singularity of the 'Euler disk' on a time-scale of several seconds, i.e. the time-scale on which the measurements have been performed with a reasonable accuracy.

REFERENCES

[1] P. Appell. Sur l'intégration des équations du mouvement d'un corps pesant de révolution roulant par une arête circulaire sur un plan horizontal; cas particulier du cerceau. *Rendiconti del Circolo Matematico di Palermo*, 14:1–6, 1900.

[2] M. Batista. Steady motion of a rigid disk of finite thickness on a horizontal plane. *International Journal of Non-Linear Mechanics*, 41:605–621, 2006.

[3] L. Bildsten. Viscous dissipation for Euler's disk. *Physical Review E*, 66(056309), 2002.

[4] A. V. Borisov, I. S. Mamaev, and A. A. Kilin. Dynamics of rolling disk. *Regular and Chaotic Dynamics*, 8(2):201–212, 2003.

[5] H. Caps, S. Dorbolo, S. Ponte, H. Croisier, and N. Vandewalle. Rolling and slipping motion of Euler's disk. *Physical Review E*, 69(056610), 2004.

[6] S. A. Chaplygin. On the motion of a heavy body of revolution on a horizontal plane (in Russian). *Physics Section of the Imperial Society of Friends of Physics, Anthropology and Ethnographics*, 9(1):10–16, 1897.

[7] K. Easwar, F. Rouyer, and N. Menon. Speeding to a stop: The finite-time singularity of a spinning disk. *Physical Review E*, 66(045102(R)), 2002.

[8] Ch. Glocker. *Set-Valued Force Laws, Dynamics of Non-Smooth Systems*, volume 1 of *Lecture Notes in Applied Mechanics*. Springer-Verlag, Berlin, 2001.

[9] K. L. Johnson. *Contact Mechanics*. Cambridge University Press, Cambridge, 1985.

[10] P. Kessler and O. M. O'Reilly. The ringing of Euler's disk. *Regular and Chaotic Dynamics*, 7(1):49–60, 2002.

[11] D. J. Korteweg. Extrait d'une lettre à M. Appell. *Rendiconti del Circolo Matematico di Palermo*, 14:7–8, 1900.

[12] C. Le Saux, R. I. Leine, and Ch. Glocker. Dynamics of a rolling disk in the presence of dry friction. *Journal of Nonlinear Science*, 15(1):27–61, 2005.

[13] R. I. Leine and Ch. Glocker. A set-valued force law for spatial Coulomb–Contensou friction. *European Journal of Mechanics – A/Solids*, 22:193–216, 2003.

[14] R. I. Leine, C. Le Saux, and Ch. Glocker. Friction models for the rolling disk. *Proceedings of the ENOC 2005 Conference*, August 7-12 2005. Eindhoven, CD-ROM.

[15] R. I. Leine and N. van de Wouw. *Stability and Convergence of Mechanical Systems with Unilateral Constraints*, volume 36 of *Lecture Notes in Applied and Computational Mechanics*. Springer Verlag, Berlin, 2008.

[16] A. J. McDonald and K. T. McDonald. The rolling motion of a disk on a horizontal plane. eprint: arXiv:physics/0008227v3, 2001.

[17] H. K. Moffatt. Euler's disk and its finite-time singularity. *Nature (London)*, 404:833–834, 2000.

[18] H. K. Moffatt. Moffatt replies. *Nature (London)*, 408:540, 2000.

[19] O. M. O'Reilly. The dynamics of rolling disks and sliding disks. *Nonlinear Dynamics*, 10(3):287–305, 1996.

[20] D. Petrie, J. L. Hunt, and C. G. Gray. Does the Euler disk slip during its motion? *American Journal of Physics*, 70(10):1025–1028, 2002.

[21] A. A. Stanislavsky and K. Weron. Nonlinear oscillations in the rolling motion of Euler's disk. *Physica D*, 156:247–259, 2001.

[22] G. van den Engh, P. Nelson, and J. Roach. Numismatic gyrations. *Nature (London)*, 408:540, 2000.